RSC Advances

PAPER

View Article Online
View Journal | View Issue



Cite this: *RSC Adv.*, 2025, **15**, 13681

# Hole transport layer selection for stable and efficient carbon electrode-based perovskite solar cells†

Kausar Ali Khawaja, Wenjun Xiang, Jacob Wall, Xiaoyu Gu, Lin Li and Feng Yan *

Perovskite solar cell (PSC) technology has achieved remarkable progress, with champion power conversion efficiencies (PCE) exceeding 26%. However, the long-term stability of PSCs remains a significant barrier to their widespread commercialization. Carbon-based PSCs (C-PSCs) have gained attention as a promising cost-effective and scalable production solution, replacing expensive metal electrodes and offering improved stability. Despite these advantages, C-PSCs face challenges in matching the performance of noble metal-based PSCs, particularly in terms of carrier extraction efficiency and reduced carrier recombination at the carbon/perovskite interface. The selection of hole transport materials (HTMs) is crucial for optimizing this interface, but comprehensive studies on HTM selection for C-PSCs are limited. This study systematically investigated three commonly used hole transport layers (HTLs): Spiro-OMeTAD, CuSCN, and PTAA. Our results show that Spiro-OMeTAD-based C-PSCs exhibit the best overall performance, achieving a PCE of 19.29%. CuSCN-based devices, while lower in efficiency (11.94% PCE), demonstrated superior stability, retaining approximately 60% of their initial performance after 500 hours under ambient conditions. PTAA-based devices achieved a PCE of 12.92% but exhibited significant degradation, maintaining only ~35% of their original efficiency over the same duration. These findings highlight the importance of selecting HTLs that balance performance and stability and emphasize the need for further optimization to enhance the commercial viability of C-PSCs.

Received 9th March 2025
Accepted 21st April 2025

DOI: 10.1039/d5ra01694k

rsc.li/rsc-advances



## 1. Introduction

Perovskite solar cells (PSCs) are emerging as a promising photovoltaic technology owing to their superior optoelectronic properties, such as high absorption coefficient, tunable bandgap, higher charge carrier mobility, long exciton diffusion length, and most importantly low fabrication cost.[1,2] Although perovskite solar cells are a promising and fastest-growing alternative to silicon solar cells, several limitations still hinder their commercialization.[3–5] These limitations can be broadly categorized into two factors: internal and external. The internal limitation originates from energy loss within the perovskite layer, primarily due to bulk recombination and optical losses, these losses are often attributed to trap-assisted non-radiative recombination and energy-level mismatch at the interfaces.[6,7] The external limitations arise from the degradation of the perovskite material when exposed to environmental factors such as moisture, oxygen, and heat.[8]

To address the internal limitations, an effective approach is to develop new materials or enhance the properties of existing interfaces and interlayer materials to minimize the energy losses. In fact, functionalized interfacial design not only addresses internal factors but also provides protection against external issues, thus significantly enhancing the device stability and reliability.[9,10] In the conventional structure (n–i–p) of perovskite solar cells, a key component of this strategy is the optimization of the hole transport layer (HTL). The HTL plays a crucial role in minimizing energy losses.[11–14] The key requirements for hole transport materials (HTMs) include suitable energy levels, high hole mobility, and solution processability with orthogonal solvents without damaging the pre-deposited perovskite layer.[15,16] In addition to serving as electron blocking layers, HTLs also play an important role in protecting the perovskite layer by exhibiting hydrophobic properties and guarding against exposure to moisture and oxygen.[17]

Carbon-based perovskite solar cells (C-PSCs) have gained significant attention in recent years, achieving PCE > 20%, in which carbon materials are used as charge collectors replacing the traditional expensive metal electrodes such as Ag and Au.[18] Planar C-PSCs exhibit many advantages, including simple manufacturing processes, compatibility with flexible substrates, low energy consumption, reduced production cost, and large-scale fabrication.[19,20] Carbon materials bring extra advantages,

*Materials Science and Engineering Program, School for Engineering of Matter, Transport and Energy, Arizona State University, Tempe, AZ, 85287, USA. E-mail: fengyan@asu.edu*

† Electronic supplementary information (ESI) available. See DOI: https://doi.org/10.1039/d5ra01694k

such as abundant availability, high electrochemical stability, efficient hole extraction, and low fabrication cost with simple fabrication techniques.[21–23] Moreover, carbon materials are highly hydrophobic and chemically inert, which can significantly improve the stability of PSCs in an ambient environment.[24,25] In addition to these advantages, recent studies have also highlighted the role of mobile ion migration in the degradation of metal halide perovskite (MHP) devices. Penukula *et al.* systematically demonstrated, using transient dark current measurements, that both device architecture and electrode composition significantly influence ionic dynamics. Their findings showed that inert carbon electrodes can reduce the mobile ion concentration ($N_o$) by nearly two orders of magnitude compared to reactive metal electrodes like silver, while also enhancing mechanical robustness as indicated by increased fracture energy ($G_c$). This ionic suppression further supports the long-term operational stability of C-PSC configurations.[26]

Nevertheless, despite the numerous advantages of C-PSCs, several critical issues remain unsolved, such as low carrier extraction, increased carrier recombination, and poor energy band alignment at the perovskite/carbon interface, all of which adversely impact the device performance.[27,28] Several methods have been adopted to improve the intrinsic properties of carbon layer and achieve favorable carbon/perovskite interfacial contacts. However, the PCEs of these devices still lag behind the traditional metal electrode-based PSCs due to the undesirable interface charge recombination. To address this issue, introduction of HTMs between the carbon and perovskite layer has been proved effective in mitigating interfacial issues in planar n–i–p C-PSCs.[29–31] Various HTMs have been adopted for C-PSCs to improve their efficiency. For example, Spiro-OMeTAD, a prevalent HTM in conventional PSCs, has demonstrated high PCE above 20% in C-PSCs.[18,32] Poly(3-hexylthiophene-2,5-diyl) (P3HT) is also commonly used HTL in C-PSCs owing to its suitable energy level alignment, which further suppress the carrier recombination with high hole transport rate.[33,34] Copper thiocyanate (CuSCN), a hydrophobic inorganic HTM, has also shown effectiveness in increasing the PCE as well as enhancing the stability of C-PSCs.[35–37]

While various HTMs such as Spiro-OMeTAD, PTAA, and CuSCN have been explored in carbon-based devices—each demonstrating unique advantages in efficiency or stability—most studies have focused on single-material demonstrations rather than comparative analysis under consistent architectures. For example, as noted earlier, Yang *et al.* showed that CuSCN offers improved stability compared to Spiro-OMeTAD, while Zhang *et al.* demonstrated enhanced operational durability using dopant-free PTAA with SWCNTs.[37,38] These findings underscore the importance of HTL selection, but a direct side-by-side evaluation of commonly used HTLs in a planar C-PSC configuration remains limited.

In our work, we address this gap by systematically investigating three commonly used HTLs—Spiro-OMeTAD, CuSCN, and PTAA—in carbon-based planar PSCs, including a control device without an HTL. Our findings reveal that Spiro-OMeTAD-based devices deliver the highest performance, achieving a superior fill factor (FF) and PCE (up to 19.29%), followed by PTAA and then CuSCN. Notably, while CuSCN-based devices exhibit lower PCEs, they demonstrate the greatest durability, with Spiro-OMeTAD showing moderate stability and PTAA the least. These results highlight the possibility of simultaneously enhancing efficiency and stability through careful selection and optimization of HTMs, thereby advancing the development of low-cost, large-area carbon-based perovskite solar cells.

## 2. Experimental section

### 2.1 Materials

$PbI_2$ (Sigma-Aldrich, 99.999%), $PbBr_2$ (Alfa Aesar, 99.98%), formamidinium iodide (FAI, GreatCellSolar), methylammonium bromide (MABr, GreatCellSolar), CsI (BeanTown Chemical, 99.9%), SnCl2·2H2O (Acros Organics, 97%), and thiourea (Alfa Aesar, 99%) were used without further purification. Dimethyl sulfoxide (DMSO) and dimethyl formamide (DMF) were purchased from Sigma-Aldrich and used as received. Spiro-OMeTAD, lithium bis(trifluoromethylsulfonyl)imide (Li-TFSI), 4-*tert*-butylpyridine (tBP), and chlorobenzene were purchased from Sigma-Aldrich. Carbon paste was purchased from Guangzhou Saidi technology development Co. Ltd, China.

### 2.2 Device fabrication

The ITO substrates were cleaned by successively sonicating in detergent solution, deionized water, acetone, and IPA followed by 30 min of UV-ozone treatment. $SnO_2$ (2.67%) colloid precursor solution was spin-coated on the cleaned ITO substrates at 3000 rpm for the 30 s. These substrates were then annealed at 150 °C for 1 hour and were then transferred to a nitrogen-filled glovebox after a 10-minute UV-ozone treatment. The triple cation perovskite ($Cs_{0.05}FA_{0.85}MA_{0.1}I_{2.55}Br_{0.45}$, 1.4 M) precursor was then deposited by a two-step spin-coating procedure: 1000 rpm 10 s followed by 5000 rpm 30 s. 600 μl diethyl ether was then dropped onto the spinning substrates 25 s before the end of spin-coating. Spiro-OMeTAD precursor solution was prepared by dissolving 72.3 mg of Spiro-OMeTAD, 28.8 μL of tBP, and 17.5 μL of Li-TFSI solution (520 mg of Li-TFSI in 1 mL acetonitrile) in 1 mL of chlorobenzene. This solution was then spin-coated on the annealed perovskite films at 3000 rpm for 30 s. CuSCN precursor solution was prepared by dissolving 35.1 mg of CuSCN in 1 mL of diethyl sulfide and stirred overnight prior to use. This prepared solution was spin coated on annealed perovskite films at 3000 rpm for 30 s. PTAA solution was prepared by dissolving 10.1 mg of PTAA, 4 μL of TBP and 75 μL of LiTFSI (170 mg of Li-TFSI in 1 mL acetonitrile). This solution was spin coated on annealed perovskite films at 3000 rpm for 30 s. The free-standing carbon film (FSC) electrode was prepared by the solvent exchange technique.[34] Briefly, the commercial carbon paste was applied onto a glass substrate using the doctor-blading technique. The resulting wet film was then immersed in ethanol to remove residual solvent through a solvent-exchange process. Afterward, the film was dried for several minutes using a dry air pump. This dried carbon electrode film was stored in a dry box for 48 hours

before use. Once fully dried, circular pieces with an area of 0.08 $cm^2$ were cut out using a hole punch. These pieces were then adhered onto the devices using hot press on top of the Spiro-OMeTAD film, completing the device.

### 2.3 Device characterization

The microscopic morphology of the electrodes was studied using a Thermo Scientific Apreo scanning electron microscope. The electrical characterization of the fabricated PSCs with an active area of 0.08 $cm^2$ was recorded using a solar simulator (Newport, Oriel Class AAA 94063A) with a Keithley 2420 source meter under simulated AM 1.5G (100 mW $cm^{-2}$) solar irradiation. The light intensity was calibrated using a silicon reference cell (Newport, 91150V, certified by National Renewable Energy Lab). The parameters were measured from 1.5 to −0.5 V with a scan rate of 100 mV $s^{-1}$. The EQE was obtained by an EnliTech QE measurement system. The capacitance–voltage (*C–V*) measurement was performed in the dark at room temperature using a Keithley 4200 semiconductor parameter analyzer (Tektronix 4200A-SCS, USA) where the DC bias voltage was swept from −0.5 to 1.5 V with a step size of 0.02 V. The EIS measurement was conducted with a Solartron Analytical 1260 impedance analyzer at a bias potential of 0.5 V in the dark with the frequency ranging from 1 Hz to 1 MHz. The contact angle was measured using a contact angle goniometer from Ossila.

## 3. Results and discussion

Fig. 1a shows the conventional device structure of C-PSCs used in this study, Fig. 1b shows the chemical structure of Spiro-OMeTAD, CuSCN and PTAA and Fig. 1c shows the energy band diagram of each layer present in the device structure mainly presenting the hole transport layers. The highest occupied molecular orbital (HUMO) level of Spiro-OMeTAD is −5.12 eV, CuSCN is −5.3 eV and PTAA is −5.1 eV. As compared to the valence band of perovskite layer −5.21 eV and Fermi level of carbon (−5.0 eV), the energy gap difference at HTL/carbon interface is low with Spiro-OMeTAD and PTAA then CuSCN. This small energy gap suggests a lower energy barrier for hole transfer, which could lead to improved charge transfer with potentially less recombination, enhancing the performance of the devices. The interface properties of HTLs and carbon electrodes were observed by DC current–voltage (*I–V*) measurement as shown in Fig. 1d. The device structure is depicted in the insert of Fig. 1d, where a HTL is sandwiched between ITO and carbon electrode. An ohmic contact has been formed between all HTLs and carbon electrodes, as evidenced by the linear *I–V* curve measurement ranging from −0.5 to 0.5 V. A higher slope is indicative of a highly conductive interface and *vice versa*. Fig. 1e shows the *I–V* slope and calculated interface resistance of the three HTLs. Among the three studied HTLs, PTAA film gives the highest *I–V* curve slope with a resistance value of 20.7 kΩ, followed by the Spiro-OMeTAD with a resistance value of 26.6 kΩ, and CuSCN with the lowest *I–V* curve slope generating the highest resistance of 136 kΩ. The values of HTL's resistances imply that PTAA/carbon interface is the most conductive as compared to other HTL/carbon interfaces, with CuSCN/carbon interface showing the lowest conductivity. The transmittance curves of perovskite underneath HTL layers, Fig. 1f show the transmittance of HTL layers. This slight change in transmission behavior could be due to the mild thickness difference arising in the perovskite layer during the device fabrication process but the effect appears mild which means its effect on device performance could be nominal and can be neglected.

To study the surface coverage of the perovskite layer with various HTLs, X-ray diffraction (XRD), and scanning electron microscopy (SEM) were employed to characterize the perovskite

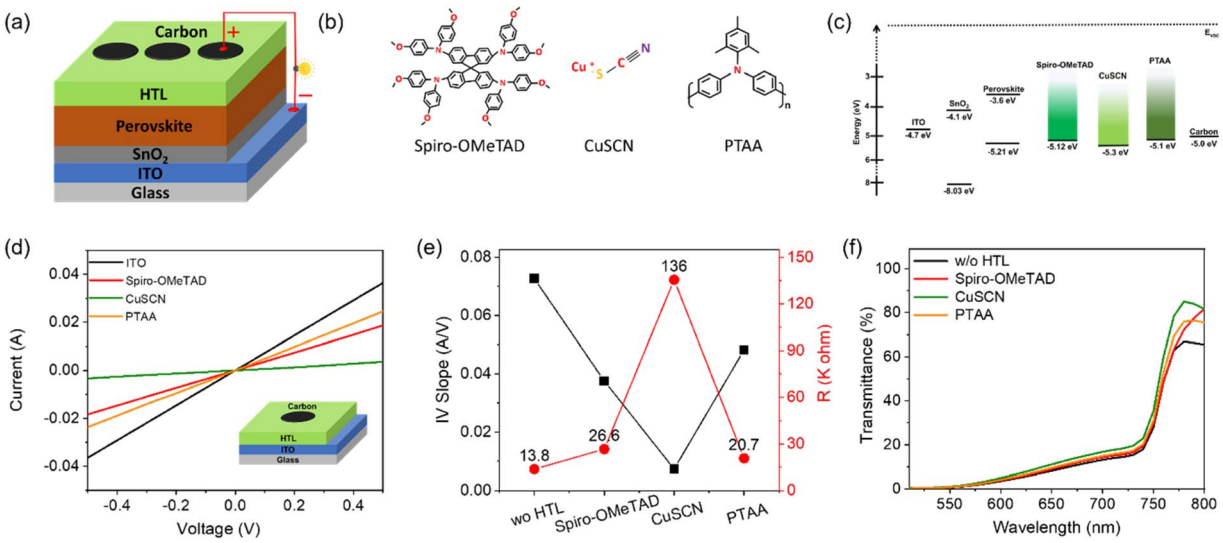


Fig. 1 (a) Device structure of C-PSCs. (b) HTLs molecular structure, (Spiro-OMeTAD, CuSCN and, PTAA), and (c) band diagram of HTLs compared to the others layers of the device. (d) IV curve of HTL device only (ITO/HTL/Carbon), (e) slope and resistance calculated from HTL on top of ITO, only IV curve and (f) transmittance of different HTL on top of perovskite layer.

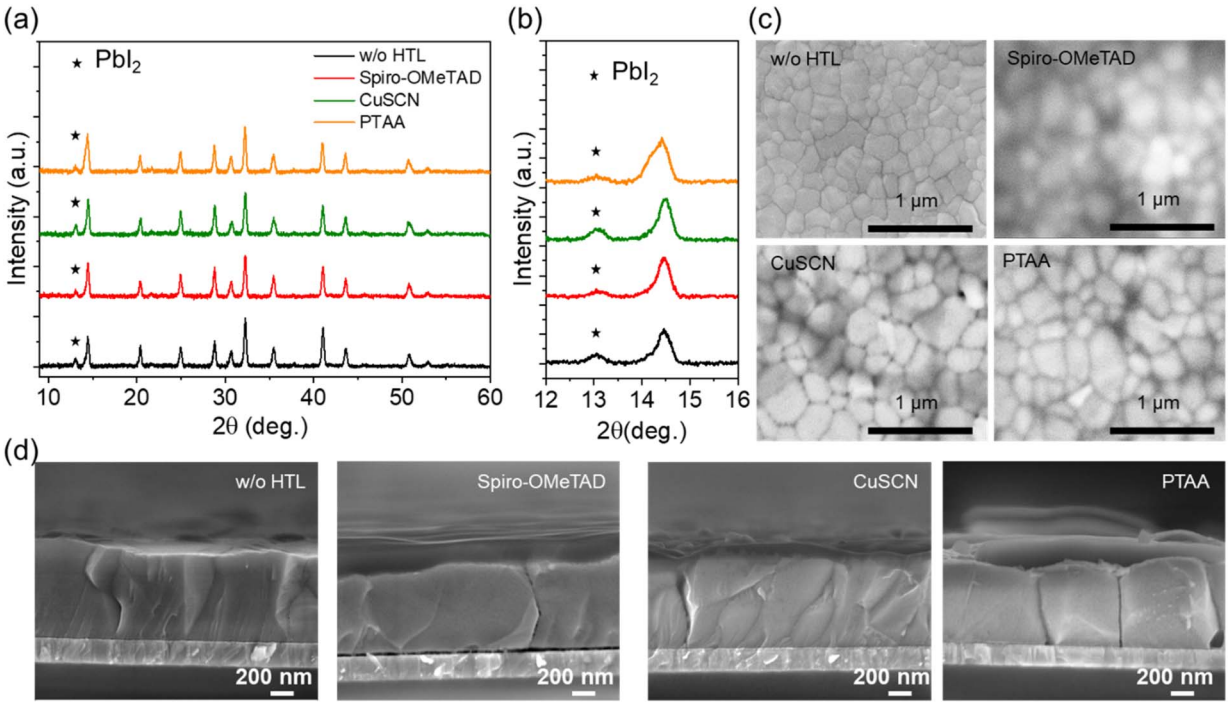





Fig. 2 (a) X-ray diffraction (XRD) of perovskite/HTL layers and (b) zoom-in region of $PbI_2$ peaks. (c) Top-view and (d) cross sectional scanning electron microscopy (SEM) of perovskite layer underneath HTLs.

layer after coating with HTLs. As shown in Fig. 2a, all of the as-deposited perovskite films, despite various HTLs, present similar perovskite cubic crystal structures, where the dominant peaks with $2\theta$ at 14.16, 20.10, and 31.9° were indexed to the triple-ion perovskite crystal plane of (001), (011) and (012), respectively. It suggests that the HTLs did not change the lattice parameters or generate a new phase on top of the perovskite layer. Fig. 2b shows that the $PbI_2$ peak intensity appears to be suppressed on these perovskite surfaces using Spiro-OMeTAD and PTAA. The suppression of the $PbI_2$ peak indicates better coverage of perovskite film using Spiro-OMeTAD and PTAA, while a strong $PbI_2$ peak for the CuSCN sample reveals poor surface coverage. Moreover, the surface morphology of these HTLs on the perovskite film has been recorded using SEM, as shown in Fig. 2c. The dark boundary lines suggest the development of nonuniformity at the perovskite/CuSCN interface, Fig. S1c, g and k, ESI.† This non-uniformity may originate from the spin coating process during the deposition of the inorganic CuSCN particles on the surface of the perovskite. The resulting low surface coverage of perovskite can lead to undesired contact between the top electrode and perovskite and therefore induce charge recombination at the interface. The thickness of the HTLs has been characterized using the cross sectional SEM as shown in Fig. 2d, where the thickness for the Spiro-OMeTAD is 200 nm, CuSCN is 100 nm and PTAA is 200 nm, respectively.

To probe the hole-extraction properties of HTLs, steady-state photoluminescence (PL) and time-resolved PL (TRPL) were conducted on perovskite/HTL films. Note that the perovskite layer was directly deposition on the glass slides without an electron transport layer to evaluate the carrier transport behavior between the pristine perovskite layer and hole transport layer. Compared with the pristine perovskite, the significant PL quench in all three HTL samples shown in Fig. 3a proves the facilitated charge transfer from perovskite to carbon electrode in C-PSCs after insertion of HTL, prohibiting recombination at the interface. TRPL spectra of perovskites with different HTLs are shown in Fig. 3b, the corresponding lifetime are extracted by fitting the spectra with following equation:

$$I(t) = \Sigma(A_i \exp(-t/\tau_i)) + C \quad (1)$$

where $A_i$ and $\tau_i$ represent the amplitude and lifetime of each decay component, respectively, and $C$ is a constant for the baseline offset. As shown in Table S2 (ESI),† the carrier lifetime of the pristine perovskite film is approximately 1.3 μs. Upon incorporating HTLs, a significant reduction in lifetime is observed, indicative of enhanced charge extraction. The Spiro-OMeTAD-based device shows the shortest lifetime of 23.2 ns, followed by PTAA at 46.4 ns, and CuSCN at 195.0 ns. The shorter carrier lifetimes for Spiro-OMeTAD and PTAA indicate more efficient hole extraction and suppressed radiative recombination at the perovskite/HTL interface, aligning with their superior device performance. In contrast, the longer lifetime for CuSCN suggests slower charge transfer and increased recombination losses, which contributes to its lower PCE. These observations are consistent with previous studies; Su *et al.* reported rapid charge extraction in Spiro-OMeTAD-based systems,[32] while Wu *et al.* noted slower interfacial kinetics for CuSCN due to its inorganic nature.[36] The intermediate behavior

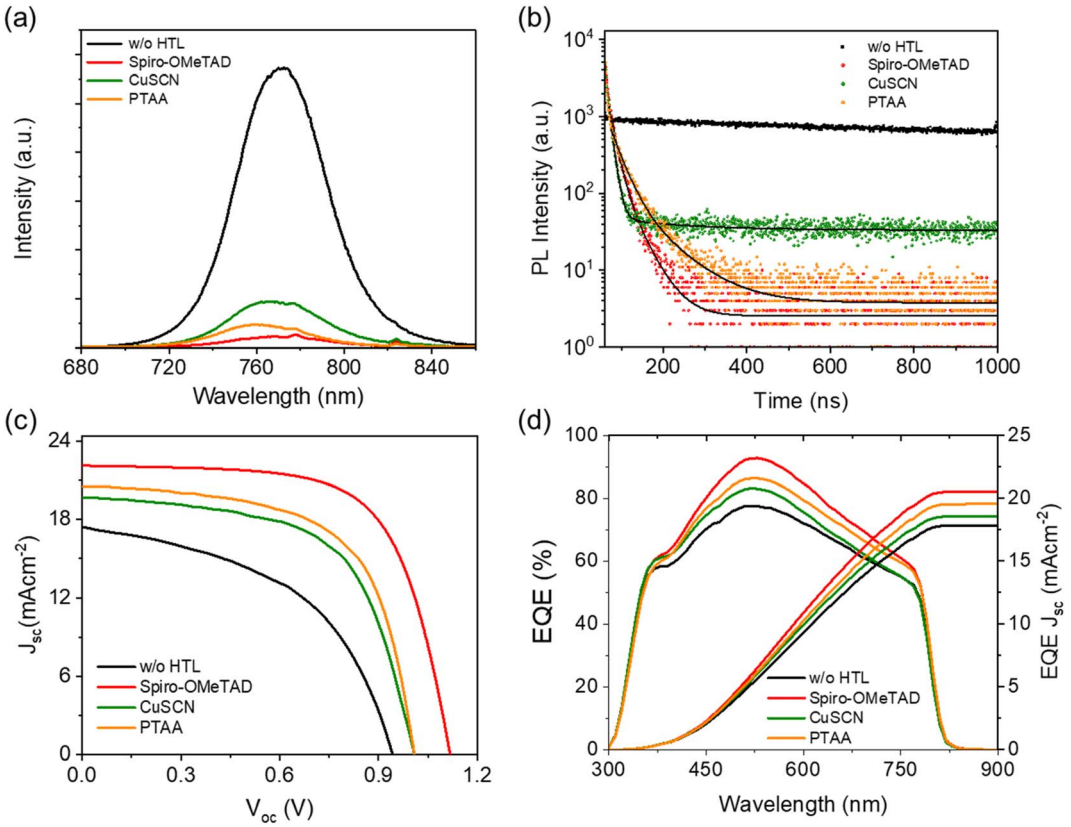


Fig. 3 (a) Photoluminescence spectra and (b) time-resolved photoluminescence spectra curves of perovskite with different HTLs. (c) Current density–voltage curves, and (d) external quantum efficiency (EQE) spectra for carbon-based PSCs with different HTLs.

of PTAA also aligns with Zhang *et al.*'s findings on moderate charge transfer dynamics in dopant-free PTAA systems.[38] Overall, the TRPL results reinforce that efficient interfacial charge separation is a key driver of the higher performance observed in Spiro-OMeTAD and PTAA-based devices compared to CuSCN.

Fig. 3c presents the *J*–*V* curves of the champion devices based on each HTL, with the corresponding photovoltaic parameters summarized in Table 1. Among the three, the Spiro-OMeTAD-based C-PSC exhibited the highest performance, achieving a PCE of 19.29%, with a short-circuit current density ($J_{sc}$) of 23.02 mA cm$^{-2}$, an open-circuit voltage ($V_{oc}$) of 1.15 V, and a fill factor (FF) of 72.97%. This performance surpasses that reported by Yang *et al.*, who demonstrated a PCE of ~17.5% in planar C-PSCs using Spiro-OMeTAD.[35] suggesting that our optimized perovskite composition and improved interface engineering resulted in more efficient hole extraction. The PTAA-based device achieved a PCE of 12.92%, with $J_{sc}$ of 20.55 mA cm$^{-2}$, $V_{oc}$ of 1.05 V, and FF of 62.62%, which aligns well with the ~16.76% PCE reported by Zhang *et al.* using dopant-free PTAA with single-walled carbon nanotube (SWCNT) electrodes,[38] considering the architectural differences. In contrast, the CuSCN-based device delivered a lower PCE of 11.94%, with a $V_{oc}$ of 1.01 V, $J_{sc}$ of 19.70 mA cm$^{-2}$, and FF of 60.03%, which is comparable to the 12–13% efficiency range reported by Wu *et al.* for CuSCN-based C-PSCs.[36] The superior performance of Spiro-OMeTAD and PTAA-based devices in our study can be attributed to their more favorable energy alignment and efficient charge extraction at the perovskite/HTL/carbon interface, as supported by TRPL analysis in Fig. 3b, which indicates lower recombination rates. A statistical comparison of device parameters is further illustrated in Fig. 4, reinforcing that Spiro-OMeTAD delivers the highest overall performance, CuSCN contributes to stable but lower-performing devices, and PTAA represents a moderate trade-off between efficiency and stability.

Table 1 Current density–voltage (*J*–*V*) parameters of champion devices of each HTL

| HTL | $V_{oc}$ (V) | $J_{sc}$ (mA cm$^{-2}$) | EQE $J_{sc}$ (mA cm$^{-2}$) | FF (%) | PCE (%) |
|---|---|---|---|---|---|
| w/o HTL | 0.94 | 17.42 | 17.82 | 49.14 | 8.07 |
| Spiro-OMeTAD | 1.15 | 23.02 | 20.53 | 72.97 | 19.29 |
| CuSCN | 1.01 | 19.70 | 18.56 | 60.03 | 11.94 |
| PTAA | 1.05 | 20.55 | 19.53 | 62.62 | 12.92 |

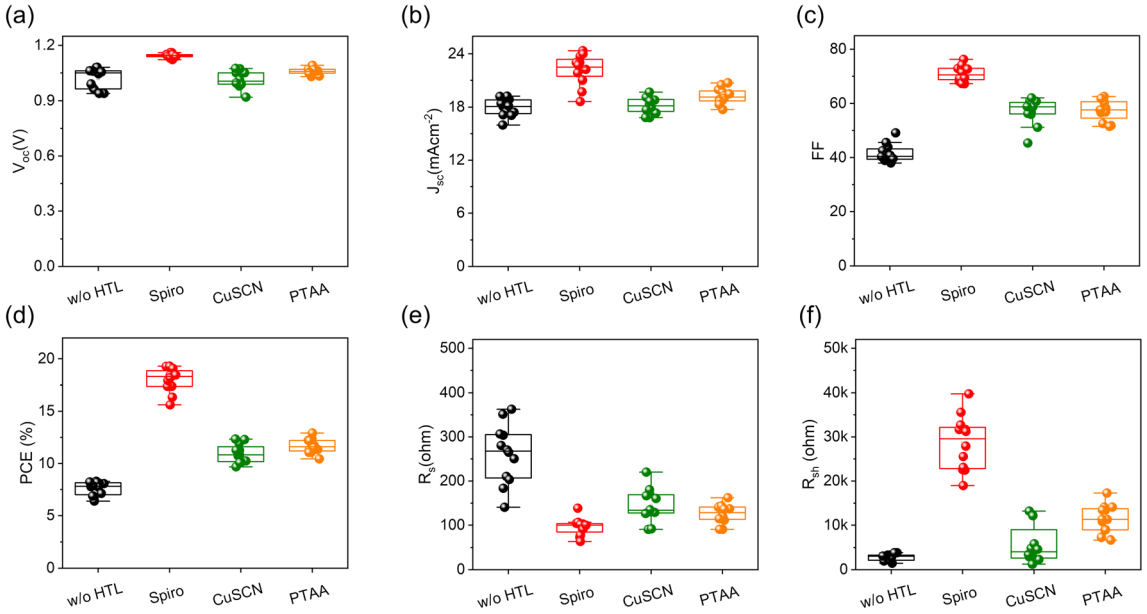


Fig. 4 Statistical distribution of key photovoltaic parameters for carbon-based perovskite solar cells (C-PSCs) incorporating different hole transport layers (HTLs): (a) open-circuit voltage ($V_{oc}$), (b) short-circuit current density ($J_{sc}$), (c) fill factor (FF), (d) power conversion efficiency (PCE), (e) series resistance ($R_s$), and (f) shunt resistance ($R_{sh}$).

To further investigate the recombination process associated with the charge transfer in each of the three HTL based devices, capacitance–voltage ($C$–$V$) measurements were performed in ESI Fig. S2a.† Fig. S2a† shows the Mott–Schottky plot depicting $1/C^2$ *versus* voltage of the solar cell under dark conditions. The governing equation for built-in potential and charge carrier concentration is determined using eqn (2):

$$1/C^2 = 2(V_{bi} - V)/q''\varepsilon\varepsilon_o N \quad (2)$$

where $C$ is the capacitance, $V_{bi}$ is the built-in potential, $V$ is the applied voltage, $q''$ is the elementary charge, $\varepsilon$ is the relative permittivity, $\varepsilon_o$ is the vacuum permittivity, and $N$ is the charge concentration. The built-in potentials deduced from the intercepts of the $1/C^2$–$V$ curves were 1.15, 1.22, 0.91 and 1.21 V for w/o HTL, Spiro-OMeTAD, CuSCN and PTAA-based devices, respectively. The increased built-in potential in Spiro-OMeTAD and PTAA devices indicates stronger charge separation driving force which contributes to higher $V_{oc}$ and fill factor and thus improved device performance. Whereas the low built-in potential in CuSCN device indicates a weak driving force, hinders charge separation and therefore promotes recombination, resulting in lower device performance. Electrochemical impedance spectroscopy (EIS) was carried out to further provide insight into the charge transport processes (ESI Fig. S2b†). Fig. S2b† shows the Nyquist plots of devices based on various HTLs measured with frequencies ranging from 1 MHz to 1 Hz, with fitted models based on the equivalent circuit shown in the inset. $R_s$ accounts for the series resistance encompasses the resistance of the materials and back/front contacts, which is in series with charge transport resistance ($R_{ct}$). Only one semicircle at a lower frequency could be distinguished in the Nyquist plots which are attributed to the charge transfer resistance ($R_{ct}$) at the perovskite/HTL interface in the solar cell. Device based on Spiro-OMeTAD showed a smaller semicircle diameter then PTAA and CuSCN, *i.e.* lower $R_{ct}$, indicates better charge transfer and prohibited recombination for devices with Spiro-OMeTAD, followed by PTAA and CuSCN. This finding aligns well with the trend observed in the $J$–$V$ test, where Spiro-OMeTAD devices exhibit the highest performance, followed by PTAA in second place, and CuSCN displaying the lowest performance.

Fig. 5a shows the schematic diagram of the carbon encapsulation of the perovskite layer. The underneath layers were etched along the corners allowing the carbon to get attached to the ITO directly during the hot press and thus encapsulating the whole perovskite layer as well as charge transport layers from direct exposure to air and water vapor. Optical pictures of perovskite solar cells were taken to observe the degradation with various HTLs after encapsulating with a carbon layer by exposing them to air for several days at room temperature (Fig. 5b), followed by placing them on hot plate at 85 °C for several minutes (Fig. 5c), and then under continuous light illumination of AM 1.5G simulated sunlight at 95 °C for several hours (Fig. 5d). The result shows that the perovskite layers did not appear to show any degradation when placed in the air or on a hot plate. However, after exposure to continuous light illumination (Fig. 5d), the perovskite layers appear to start degrading within hours and completely degraded within 24 hours with no visible difference from each condition. The degradation is due to the intrinsic deterioration produced by thermal stress and illumination.[9]

To further test the encapsulating capability of the carbon layer with different HTLs, the devices were immersed in water completely to value the water resistivity by checking the

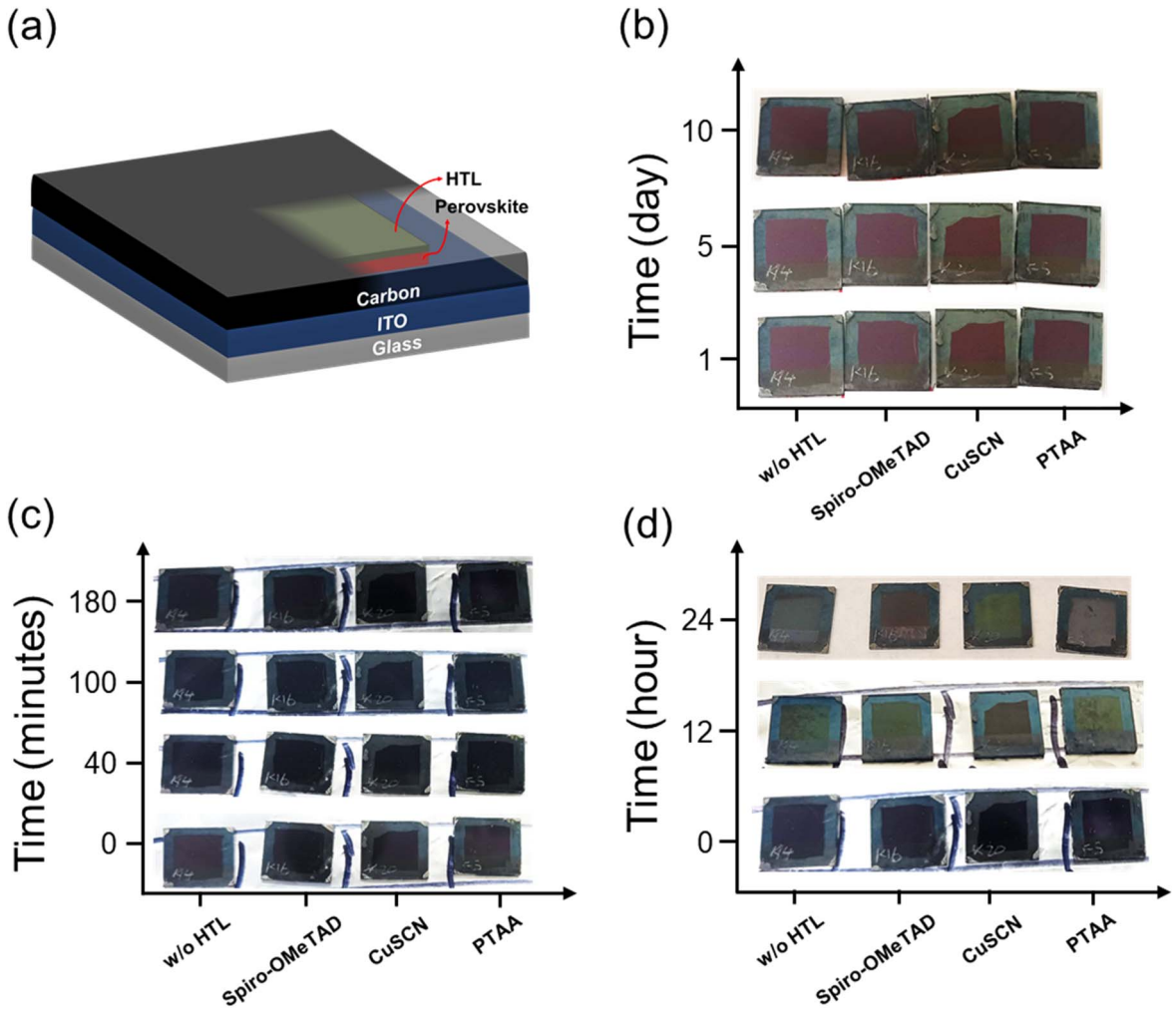


Fig. 5 Optical pictures of the stability test condition. (a) Schematic diagram of carbon electrode encapsulation of perovskite layer. (b) Optical picture of cells exposed to air at room temperature. (c) For the same cells anneal at 85 °C in air, and (d) Light soaking at 95 °C under AM 1.5G simulated sunlight illumination.

perovskite degradation rate. The water immersion experiment serves as an accelerated aging test to stimulate extreme moisture exposure. Optical images of encapsulated samples immersed in water at duration time of 0 min, 40 min, and 120 min were recorded, as shown in Fig. 6a. The difference observed among the devices highlight the effectiveness of the HTLs in enhancing stability. The color shift from black to yellow in perovskite films is widely recognized as a sign of degradation, typically caused by hydration and the formation of lead iodide as water breaks down the perovskite material. The slower color change observed in CuSCN and Spiro HTL-based devices, when immersed in water, indicates that these HTLs act as effective barriers, slowing water penetration into the perovskite layer and delaying degradation. In contrast, the PTAA and HTL-free devices degrade more quickly, showing less effectiveness in moisture protection. Meanwhile, contact angle of water droplets on each HTL was also measured to check their hydrophobicity, with the optical images and corresponding data depicted in the first line of Fig. 6b and c. The CuSCN sample possesses the highest contact angle (80.7°), followed by Spiro-OMeTAD (67.5°) and PTAA (55.7°), which implies the order of hydrophobic properties of these materials on perovskite film. The result is well agreed with the water immerse experiment, the reference device without HTL and the device with PTAA showed partial or complete degradation after 120 minutes of immersion, while Spiro-OMeTAD and the CuSCN-based devices showed effective protection of the perovskite layer from water (Fig. S3†). Since the carbon electrode fully covers the top of the device, it provides extra protection against moisture from above. The damage visible through the glass side is primarily due to water entering from the edges, as seen from the yellowing around the perimeter, indicating degraded perovskite in these areas. In conclusion, it was observed that carbon film together with CuSCN and Spiro provide better encapsulation and less direct exposure to water thereby improving the stability of the device. In conclusion, it was observed that carbon film together with CuSCN and Spiro provide better encapsulation and less direct exposure to water thereby improving the stability of the device.

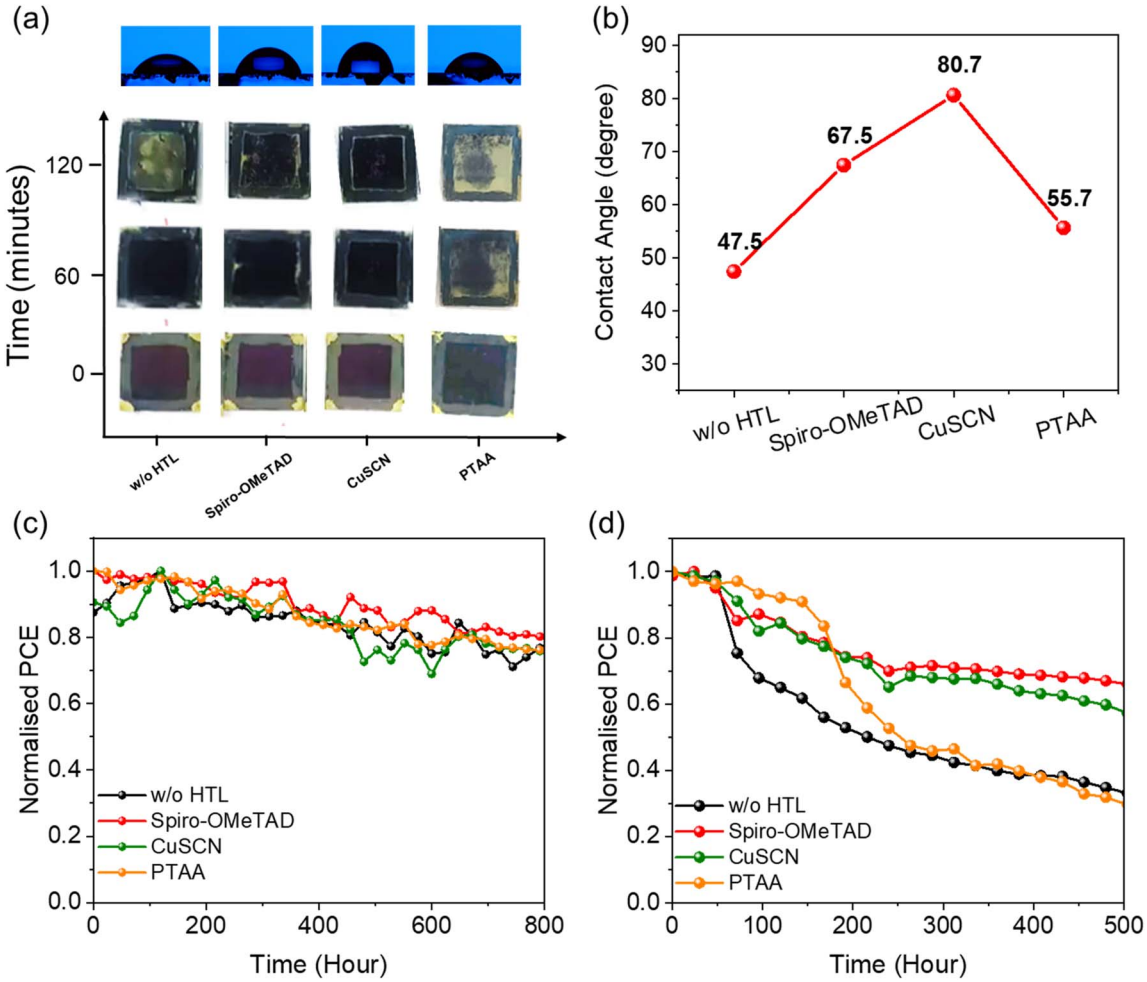


Fig. 6 (a) Water droplets on different perovskite/HTLs, and corresponding optical images of encapsulated samples immersed in water with different duration. (b) Contact angle of different perovskite/HTLs. Normalized PCE of PSC-HTM-free carbon-based perovskite solar cells with different HTLs: (c) measured over 800 hours in an $N_2$ atmosphere and (d) measured over 500 hours in an ambient atmosphere with humidity below 5% RH.

This also shows that the hydrophobicity of HTLs also plays an effective role in enhancing the encapsulation of perovskite layer in C-PSC devices.

The stability behavior of perovskite solar cells (PSCs) employing different hole transport layers (HTLs) under varying storage and environmental conditions is presented in Fig. 6c and d, which track the normalized power conversion efficiency (PCE) over time. Under inert $N_2$ glovebox conditions without encapsulation (Fig. 6c), Spiro-OMeTAD-based devices exhibited the best stability, retaining ~80% of their initial PCE after 800 hours. PTAA devices maintained ~70%, followed by CuSCN with ~60%, while HTL-free devices showed the poorest stability, dropping to ~45% over the same period.

Under ambient conditions at ~5% relative humidity (Fig. 6d), Spiro-OMeTAD again outperformed others, retaining ~70% of its initial efficiency after 500 hours—consistent with previous findings by Su *et al.*, who reported moderate degradation in doped Spiro-OMeTAD under illumination.[32] CuSCN-based devices retained ~60% of their PCE, aligning well with Wu *et al.*, who observed >85% retention over 500 hours at 50% RH.[36] PTAA devices showed a marked decline, retaining only ~35% efficiency, while devices without HTLs stabilized around the same value after just 200 hours. These trends mirror the results reported by Zhang *et al.*,[38] who found that PTAA without dopant engineering or advanced electrode configurations suffers from accelerated degradation.

Overall, these results highlight that Spiro-OMeTAD and CuSCN offer superior environmental stability compared to PTAA or HTL-free devices, reinforcing the conclusion that HTL selection plays a critical role in both initial performance and long-term durability of carbon-based PSCs.

## 4. Conclusions

In summary, three widely used Hole Transport Layers (HTLs)—Spiro-OMeTAD, CuSCN, and PTAA—were studied in conjunction with carbon-based perovskite solar cells (C-PSCs) to evaluate their stability and efficiency. Spiro-OMeTAD-based C-PSCs

exhibited the best performance, achieving a PCE of 19.29%, attributed to favorable energy alignment and efficient charge extraction. CuSCN-based devices, while showing a lower PCE of 11.94%, demonstrated superior stability, retaining ~60% efficiency after 500 hours in ambient air. PTAA-based devices achieved moderate efficiency (12.92%) but degraded more rapidly, retaining only ~35%. These findings highlight the importance of optimizing HTL selection and suggest that future improvements could be realized through dopant-free formulations, hybrid HTLs, and improved encapsulation strategies to further enhance the durability and performance of C-PSCs.

## Data availability

The materials and data that support the findings of this study are available from the corresponding author upon reasonable request.

## Author contributions

KK: methodology, investigation, and writing – original draft. JW, WJX: investigation, LL, X. G. writing review. FY: conceptualization, methodology, funding acquisition, supervision, writing-review & editing.

## Conflicts of interest

The authors declare no competing financial interest.

## Acknowledgements

This material is based upon work supported by the U.S. Department of Energy's Office of Energy Efficiency and Renewable Energy (EERE) under the Solar Energy Technologies Office Award Number DE-EE0009833. The National Science Foundation supports this work under contract No. DMR 2330738, ECCS-2413632, CMMI-2226918, CMMI-2330728, and TI-2329871.

## References

1 A. K. Jena, A. Kulkarni and T. Miyasaka, *Chem. Rev.*, 2019, **119**, 3036–3103.
2 J. Y. Kim, J.-W. Lee, H. S. Jung, H. Shin and N.-G. Park, *Chem. Rev.*, 2020, **120**, 7867–7918.
3 Y. Li, H. Xie, E. L. Lim, A. Hagfeldt and D. Bi, *Adv. Energy Mater.*, 2022, **12**, 2102730.
4 W. E. I. Sha, X. Ren, L. Chen and W. C. H. Choy, *Appl. Phys. Lett.*, 2015, **106**, 221104.
5 W. Shockley and H. J. Queisser, *J. Appl. Phys.*, 1961, **32**, 510–519.
6 J. Chen and N.-G. Park, *ACS Energy Lett.*, 2020, **5**, 2742–2786.
7 H. Pan, H. Shao, X. L. Zhang, Y. Shen and M. Wang, *J. Appl. Phys.*, 2021, **129**, 130904.
8 J. Li, R. Xia, W. Qi, X. Zhou, J. Cheng, Y. Chen, G. Hou, Y. Ding, Y. Li, Y. Zhao and X. Zhang, *J. Power Sources*, 2021, **485**, 229313.
9 D. Zhang, D. Li, Y. Hu, A. Mei and H. Han, *Commun. Mater.*, 2022, **3**, 58.
10 L. Xiang, F. Gao, Y. Cao, D. Li, Q. Liu, H. Liu and S. Li, *Org. Electron.*, 2022, **106**, 106515.
11 R. Wu, J. Meng, Y. Shi, Z. Xia, C. Yan, L. Zhang, W. Liu, J. Zhao, J. Deng and X. Zhang, *J. Mater. Chem. A*, 2024, **4**, 26.
12 S. Akin, Y. Liu, M. I. Dar, S. M. Zakeeruddin, M. Grätzel, S. Turan and S. Sonmezoglu, *J. Mater. Chem. A*, 2018, **6**, 20327–20337.
13 İ. C. Kaya, R. Ozdemir, H. Usta and S. Sonmezoglu, *J. Mater. Chem. A*, 2022, **10**, 12464–12472.
14 F. Kong, E. Güzel and S. Sonmezoglu, *Mater. Today Energy*, 2023, **35**, 101324.
15 X. Yin, Z. Song, Z. Li and W. Tang, *Energy Environ. Sci.*, 2020, **13**, 4057–4086.
16 S. Wang, A. Cabreros, Y. Yang, A. S. Hall, S. Valenzuela, Y. Luo, J.-P. Correa-Baena, M.-c. Kim, Ø. Fjeldberg, D. P. Fenning and Y. S. Meng, *Cell Rep. Phys. Sci.*, 2020, **1**, 100103.
17 S. Li, Y.-L. Cao, W.-H. Li and Z.-S. Bo, *Rare Met.*, 2021, **40**, 2712–2729.
18 H. Zhang, Y. Li, S. Tan, Z. Chen, K. Song, S. Huang, J. Shi, Y. Luo, D. Li and Q. Meng, *J. Colloid Interface Sci.*, 2022, **608**, 3151–3158.
19 S. Ko, T. Yong, S.-K. Kim, J. Y. Park, G. Lee, H. R. You, S. Han, D. Lee, S. Choi, Y. C. Choi, Y. Kim, N.-S. Lee, S. Song and J. Choi, *Sol. RRL*, 2023, **7**, 2300049.
20 P. Pradid, K. Sanglee, N. Thongprong and S. Chuangchote, *Materials*, 2021, **14**(19), 5989.
21 H. Zhang, J. Xiao, J. Shi, H. Su, Y. Luo, D. Li, H. Wu, Y.-B. Cheng and Q. Meng, *Adv. Funct. Mater.*, 2018, **28**, 1802985.
22 M. Hu, L. Liu, A. Mei, Y. Yang, T. Liu and H. Han, *J. Mater. Chem. A*, 2014, **2**, 17115–17121.
23 S. Zhu, J. Tian, J. Zhang, C. Gao and X. Liu, *ACS Appl. Energy Mater.*, 2021, **4**, 5554–5559.
24 D. Bogachuk, S. Zouhair, K. Wojciechowski, B. Yang, V. Babu, L. Wagner, B. Xu, J. Lim, S. Mastroianni, H. Pettersson, A. Hagfeldt and A. Hinsch, *Energy Environ. Sci.*, 2020, **13**, 3880–3916.
25 D. Bogachuk, B. Yang, J. Suo, D. Martineau, A. Verma, S. Narbey, M. Anaya, K. Frohna, T. Doherty, D. Müller, J. P. Herterich, S. Zouhair, A. Hagfeldt, S. D. Stranks, U. Würfel, A. Hinsch and L. Wagner, *Adv. Energy Mater.*, 2022, **12**, 2103128.
26 S. Penukula, F. Tippin, M. Li, K. A. Khawaja, F. Yan and N. Rolston, *Energy Mater.*, 2024, **4**, 26.
27 H. Chen and S. Yang, *J. Mater. Chem. A*, 2019, **7**, 15476–15490.
28 H. Chen and S. Yang, *Adv. Mater.*, 2017, **29**, 1603994.
29 S. N. Vijayaraghavan, J. Wall, H. G. Menon, X. Duan, L. Guo, A. Amin, X. Han, L. Kong, Y. Zheng, L. Li and F. Yan, *Sol. Energy*, 2021, **230**, 591–597.
30 M. Que, B. Zhang, J. Chen, X. Yin and S. Yun, *Mater. Adv.*, 2021, **2**, 5560–5579.
31 Z. Yu, W. Li, N. Cheng, Z. Liu, B. Lei, Z. Xiao, W. Zi, Z. Zhao and Y. Tu, *ACS Appl. Nano Mater.*, 2022, **5**, 10755–10762.

32 H. Su, X. Lin, Y. Wang, X. Liu, Z. Qin, Q. Shi, Q. Han, Y. Zhang and L. Han, *Sci. China:Chem.*, 2022, **65**, 1321–1329.
33 W. Yu, Y. Zou, S. Zhang, Z. Liu, C. Wu, B. Qu, Z. Chen and L. Xiao, *Mater. Futures*, 2023, **2**, 022101.
34 F. Zhao, J. Zhou, J. Tao, Y. Guo, J. Jiang and J. Chu, *J. Alloys Compd.*, 2022, **897**, 162741.
35 Y. Yang, N. D. Pham, D. Yao, L. Fan, M. T. Hoang, V. T. Tiong, Z. Wang, H. Zhu and H. Wang, *ACS Appl. Mater. Interfaces*, 2019, **11**, 28431–28441.
36 X. Wu, L. Xie, K. Lin, J. Lu, K. Wang, W. Feng, B. Fan, P. Yin and Z. Wei, *J. Mater. Chem. A*, 2019, **7**, 12236–12243.
37 Y. Yang, M. T. Hoang, D. Yao, N. D. Pham, V. T. Tiong, X. Wang and H. Wang, *J. Mater. Chem. A*, 2020, **8**, 12723–12734.
38 B.-W. Zhang, H.-S. Lin, X.-Y. Qiu, Q.-J. Shui, Y.-J. Zheng, M. Almesfer, E. I. Kauppinen, Y. Matsuo and S. Maruyama, *Carbon*, 2023, **205**, 321–327.